

GT2023-102276

The Effect of Trailing Edge Grid Resolution in Large-Eddy Simulations

Kenji Miki¹, Ali Ameri^{1,2}

¹NASA Glenn Research Center, Cleveland, OH

²The Ohio State University, Columbus, OH

ABSTRACT

Ceramic Matrix Composite (CMC) with environmental barrier coating can tolerate significantly higher temperatures compared with the conventional metal alloy blades and thus can help achieve higher thermal efficiency in gas turbine engines. Due to the complex fabrication process of CMC blades, larger blade trailing edge thicknesses and larger leading-edge radii of curvature are expected. These features significantly alter aerodynamic performance especially near the trailing edge and thus the loss profile. In previous studies, the authors used the large eddy simulation (LES) as well as the Reynolds Averaged Navier-Stokes (RANS) coupled with an intermittency function-based transition model to simulate an aerodynamics performance of three different CMC blades and compared the predictions against the data acquired at NASA Glenn Transonic Turbine Blade Cascade Rig. Although we were able to successfully predict different characteristics of aerodynamic performance among three different blades (e.g., pressure loading and integrated losses), LES consistently predicted a small recirculation bubble at the end of the suction side. This was not inconsistent with the physics of the flow, but the pressure loading, locally, near the trailing edge, and as a result, the measured wake profiles did not match the experimental data. To delve further into these issues, a new LES grid with a much finer mesh near the trailing edge was generated where the spanwise extent of the grid was increased by 50%. An LES simulation for the CMC blade with the largest trailing edge thicknesses at the high-freestream turbulence ($Tu=13\%$) condition showed that using such a mesh is necessary for LES to accurately capture the transition phenomena on the suction side. The resulting total pressure coefficient profile and the shift of the wake profile were greatly improved.

NOMENCLATURE

AUSM	Advection Upstream Splitting Method
BC	Boundary Condition
CFD	Computational Fluid Dynamics
CMC	Ceramic Matrix Composite
C_x	axial chord
FST	Freestream Turbulence
h	span
h_δ	spanwise boundary layer thickness
$L_{s,0}, L_{s,1}$	axial location of upstream and downstream measurement stations 0 and 1
LDKM	Localized Dynamic Kinetic Model
LES	Large-Eddy simulation
LPT	Low-pressure Turbine
K-H	Kelvin-Helmholtz
Ma	Mach number
RANS	Reynolds-Averaged Naiver-Stokes
Re	Reynolds number
TKE	turbulence kinetic energy
Ts	turbulent length scale
Tu	turbulence intensity
u, v, w	velocity component
X, Y, Z	Cartesian coordinate
β	Inflow flow angle

SUBSCRIPTS

0	upstream location
1	downstream location
<i>in</i>	Based on inlet conditions
<i>ex</i>	Based on exit conditions
<i>rms</i>	root mean square
<i>X</i>	Axial

Keywords: LES-LDKM, Free-stream turbulence, CMC, separation/transition

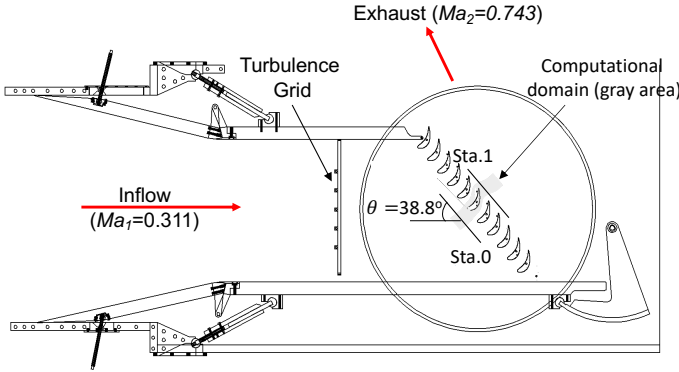


FIGURE 1: OVERVIEW OF THE EXPERIMENTAL FACILITY AT NASA GRC [1]

INTRODUCTION

Ceramic Matrix Composites (CMC) play a critical role as a next generation of blade materials owing to their tolerance for higher temperatures and reduced weight. The improved temperature tolerance enables enhanced thermal efficiency by permitting higher turbine inlet temperatures and/or reduced cooling requirement. To take advantage of thermal characteristic of CMCs while maintaining the necessary strength, it may be necessary to modify the conventional design concepts for alloy blades by having a thicker trailing edge.

Recently, Giel *et al.* experimentally studied the aerodynamics of the CMC blades and investigated the dependence of the profile loss against the free-stream turbulence (FST) intensity (Tu) and the Reynolds number (Re) [1] (See Fig.1). They varied the trailing edge thicknesses of 5%, 7% and 9% of axial chord and thereby loadings (aft- (CMC5), mid- (CMC7), and front- (CMC9) loaded designs.) Those thicknesses correspond to those produced by 2 to 4 plies of CMC for the size of the blade considered. Two sets of experimental data were acquired at two different FSTs, $Tu=0.5\%$ and 13%. Primary findings are as summarized below: In the case with $Tu=0.5\%$, CMC5 and CMC7 showed higher profile losses at low Re_{ex} ($\sim 300,000$) than CMC9. As Re increased, the losses of all the blades decreased. However, CMC9 showed the least reduction and had the largest loss at high Re_{ex} ($>1000,000$). For the high FST case, CMC9 had the highest loss regardless of Re , and the dependence of the loss on Re was less pronounced for CMC9. It was clearly demonstrated that each design of the blade showed a different degree of dependence on Re at different FST.

In the past, there have been numerous numerical studies investigating the dependence of the losses on Re under different FST conditions. They mainly employ two simulation methods for this kind of application: the Reynolds-Averaged Navier-Stokes (RANS) method and large eddy simulation (LES). For instance, Lyall, *et al.* [2], Keadle, *et al.* [3] and Arko-, *et al.* [4] used RANS to investigate the front- and aft-loaded designs at a relatively low FST ($Tu\sim 3.1\text{-}3.3\%$). It was reported that it was a

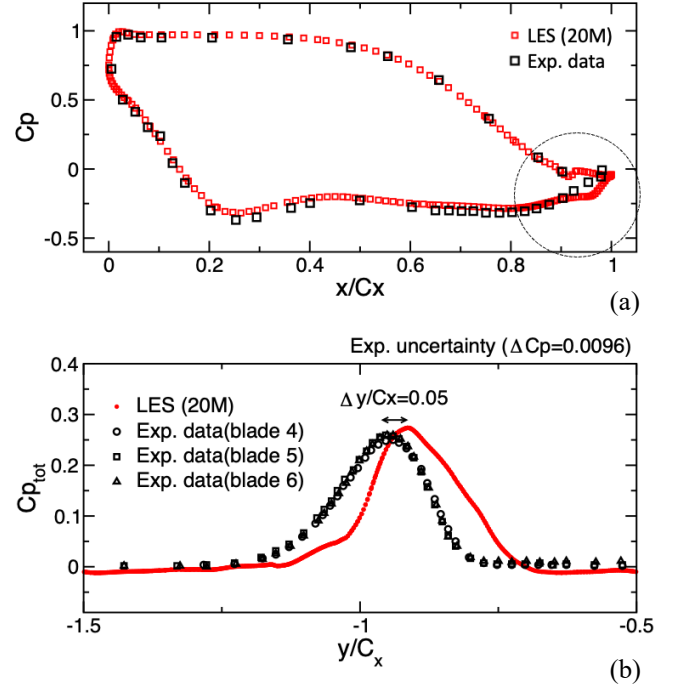


FIGURE 2: (a) MIDSPAN BLADE LOADING AND (b) WAKE PROFILE OF THE FRONT_LOADED BLADE [9]

challenge for RANS to accurately capture the suction side vortices caused by the separated shear layer using two-dimensional simulations. Vázquez, *et al.* [5] found that the loss decreased like $Re^{-0.15}$ with increasing Re for the LPT blade ($120,000 < Re < 315,000$), which is a much weaker dependence than the reported values by Giel *et al.* [1] ($Re^{-.76}$, $Re^{-0.66}$ and $Re^{-0.31}$ for the aft-, mid-, and front-loaded). Medic and Sharma [6] and Bolinches-Gisbert *et al.* [7] used LES to investigate the LPT blades with ($Tu=4\%$) and without FST for $30,000 < Re < 150,000$ and $Re \sim 50,000$, respectively. Pichler *et al.* [8] performed a grid convergence study for LPT DNS at a $Re=60,000$ with the aim of resolving the background turbulence with 18, 72 and 200 million points. They found the coarsest grid did sufficiently well in producing the separation location, pressure distribution and the wake loss profile. They used a conventional T106A profile.

Our previous studies conducted LES for $157,000 < Re < 314,500$ using both RANS and LES at the high-FST ($Tu=13\%$) [9]. It was demonstrated that both RANS and LES predicted the transition locations similarly and could capture the sensitivity to Re for the integrated loss coefficients of all the aft, mid- and front-loaded designs. However, as shown in Fig. 2 (a) and (b), there are still noticeable discrepancy seen between the predictions by LES and the data (the pressure loading and the wake profiles) in the front-loaded design. In the pressure loading profile (Fig. 2 (a)), LES predicted a small bubble at the end of the suction side, leading to a "kink" at $x/Cx = 0.95$. Also, there is a "shift" ($\Delta y/Cx=0.05$) between the wake profile and the data (see

TABLE 1: GEOMETRY AND OPERATING PARAMETERS OF CMC BLADES [1]

Geometry	Value
Chord, C_x [in]	5.119
Pitch, S [in]	5.119
Span, h [in]	6.00
Axial location of Sto 0, $L_{S,0}/C_x$	-0.87
Axial location of Sto1, $L_{S,1}/C_x$	1.20
Inlet flow angle, β , [deg.]	38.8
Trailing edge metal angle, θ , [deg.]	60.9
Leading Edge Diameter, [in]	0.885
Trailing Edge Diameter, [in]	0.46
Operating Condition	
Pressure ratio	1.442
Re_{ex}	314,500
Turbulent intensity, Tu [%]	13
Turbulent length scale, Ts/C_x	0.02

Fig.2 (b)). Although the authors rigorously followed the numerical setting and grid resolution requirements based on our past studies [10-11], these issues persisted. Please note that our past studies demonstrated that the over-estimated wake loss was due to an inadequate grid resolution, insufficiently resolving the momentum transport from the free stream turbulence while the pressure loading was accurately calculated.

In this paper, we use the above validated numerical approach to predict the pressure loading and the wake profiles of the blade design (CMC9) with the thickest trailing edge and a front-loaded design. We ran at a high Re ($=314,500$) condition with a high FST ($Tu=13\%$), hoping to resolve the aforementioned issues using the newly generated mesh. Two sets of the predictions using the original mesh (~ 20 million points) [9] and the new mesh (~ 50 million points) are compared.

EXPERIMENTAL SETUP

Figure 1 schematically shows the experimental facilities located at the NASA Glenn Transonic Turbine Blade Cascade Facility (CW-22) [1]. The clean and dry air is introduced from the GRC's 40 psig combustion air system. The design Mach

number at the inlet is 0.311, and the air passes through the turbulence grid designed to generate nearly isotropic turbulence. Some key geometrical and operational parameters are summarized in Table 1. The blades are located downstream with an incident angle, $\beta=38.8$ [deg]. Please note that the turbulence grid does not align against the blade row. Therefore, there is a noticeable pitchwise variation in Tu measured at Station 0 [12]. The inlet turbulence intensity was 13% and the pitchwise variances was $\pm 2.6\%$. The boundary layer thicknesses normalized by the half of the span are 0.24 for this test case, and thus it is reasonable to assume that the end-wall effect might be negligible. Finally, the wake losses are measured at $L_{S,1}=20\%$ axial-chords downstream of the trailing edge of the blade (Station 1).

The estimated measurement uncertainties of the pressure loading (C_p), the total pressure coefficient ($C_{p,tot}$) and the integrated kinetic energy loss coefficient (e_2) are ± 0.046 , ± 0.005 and ± 0.004 . The more detailed description of the experimental setup and the measurements are provided in [1]

NUMERICAL SETUP

As used in our previous study [9], we used the in-house code, Glenn-HT [13], which has been continuously developed over the past two decades at the NASA Glenn Research Center. It is an unsteady compressible Navier-Stokes solver that utilizes structured multi-block grids. The explicit four-stage Runge-Kutta scheme is used for achieving the 2nd order temporal accuracy. The AUSM⁺up scheme [14] coupled with the compact 2nd order limiter of the MUSCL scheme is used to evaluate the inviscid fluxes. To achieve turbulent closure for LES, the localized dynamic k -equation model (LDKM) proposed by Kim and Menon [15] is used for all test cases. The key idea of LDKM is that the model coefficients appearing in the Reynold stress as well as the turbulent kinetic energy equations are dynamically evaluated based on the assumption of the scale similarity [16]. To this end, we introduce two filters, the spatial filter ($\bar{\Delta} = (\Delta x \Delta y \Delta z)^{1/3}$) and the test filter ($\hat{\Delta} = 2\bar{\Delta}$). The validation tests of the current implementation of LDLM have been done [17-18].

TABLE 2: STATISTICS OF INCOMING TURBULENCE

LES						Exp. [12]	
$X/C_x = -0.87$						Station 0	
Tu [%]	u'_{rms}/U_0	v'_{rms}/U_0	w'_{rms}/U_0	$(u'v')^{1/2}/U_0, (u'w')^{1/2}/U_0, (v'w')^{1/2}/U_0$	< 0.001	Tu [%]	Pitch Variance [%]
11.0	0.06	0.07	0.06			12.4	± 2.6

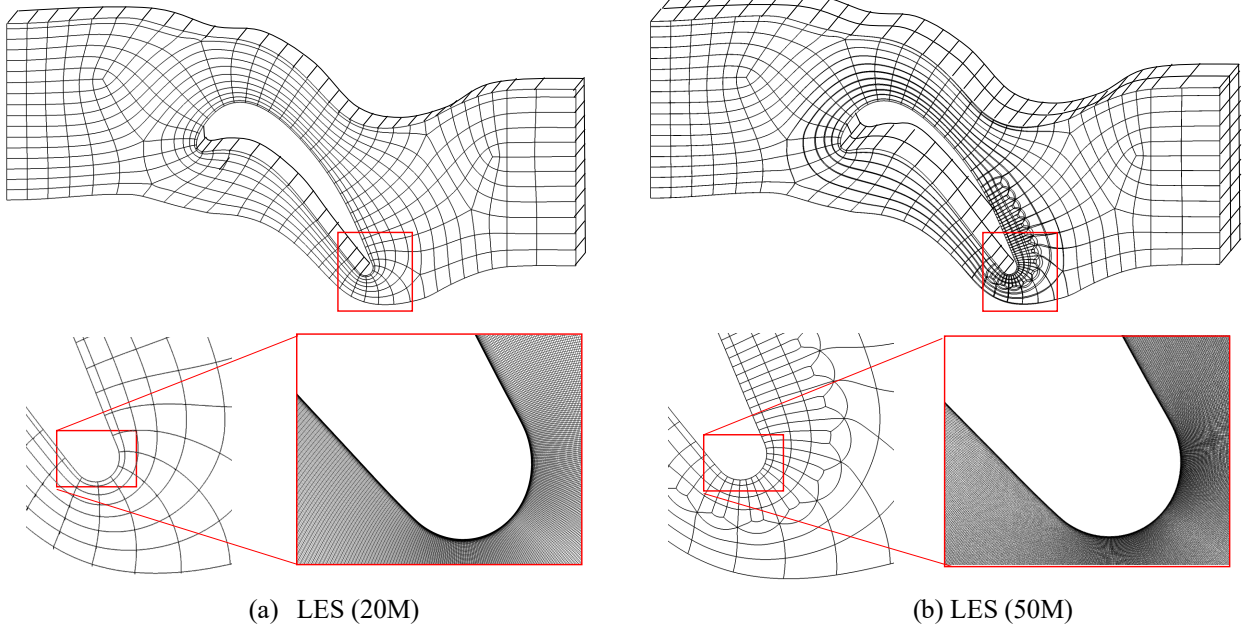


FIGURE 3: TOPOLOGY OF MESH (BLOCK BOUNDARY) AND MESH NEAR THE TRAILING OF (a) LES (20M) AND (b) LES (50M)

Boundary Condition and Mesh

Operating condition is summarized in Table 1. Considering that the boundary layer thickness is 24% of the half of the span, we considered only the midspan section of the domain and used periodic boundaries in the spanwise direction. At the inlet, we used the digital filtering approach [19] to generate a realistic, time-dependent, inlet turbulence given T_u (=13 %) and T_s/C_x (=0.02). The characteristic of the inflow turbulence at $X/C_x=-0.87$ are summarized in Table 2. It is confirmed that u'^{rms}/U_0 , v'^{rms}/U_0 , and w'^{rms}/U_0 make up isotropic incoming turbulence in this setup and the cross-components ($u'v'$, $u'w'$, and $v'w'$) are almost zero. Please note that the turbulence grid is not a part of this calculation and that the survey plane (Station 0) is not parallel to the turbulence grid. Therefore, there are some uncertainties associated with the measurements of the turbulence intensity and the length scales.

Figures 3 (a) and (b) compares two grids, one is the original grid [9] (referred to as LES (20M) herein) and the other is the newly generated grid (referred to as LES (50M)). The figures on the top row and the bottom left show the block topology. The key features of these two meshes are listed as follows:

- The resolutions of the LES (20M) and LES (50M) meshes are ~ 20 million and ~ 50 million points.
- For both meshes, the grid spacing near the wall is placed at 1.25×10^{-6} [m]. As a result, y_{I^+} is close to unity over the blade. In the midspan wall region, on the average, x_{I^+} value is of ~ 10 and z_{I^+} is of ~ 20 .

- The span of the domain is $0.2 \times C_x$ and $0.3 \times C_x$ for the LES (20M) and LES (50M) meshes.
- In the upstream region, the grid topology and resolutions are the same for both meshes. We calculated the well-known Pope criterion and found that it is less than 0.1 over most of the freestream region. In addition, the power spectral density of the normalized axial velocity component was calculated, and it was confirmed that the spectral slope followed the Kolmogorov -5/3 law [9]. The mesh resolution in the upstream region seems to be adequate to resolve the incoming high FST.
- Near the end of the suction side and the trailing edge, we locally increased the grid resolution for the LES (50M) grid three times more than the LES (20M) grid. This local refinement minimizes the increase of the total mesh count.

Recently Lee *et al.* [20] have investigated the effect of span of the computational domain (in quasi-three-dimensional LES computations) on the computed loss predictions. It was shown that the effect of the extent of the span of the computational domain is important especially for the large angle of attack. It is worth mentioning that the large trailing edge diameter (=0.46 [in]) is comparable to the half of the span of the grid, LES (20M) so that it could be possible that large structures of the flow field cannot be accurately resolved when using such a mesh.

RESULTS

We used 480 processors on Pleiades at NASA Advanced Supercomputing facilities to perform LES

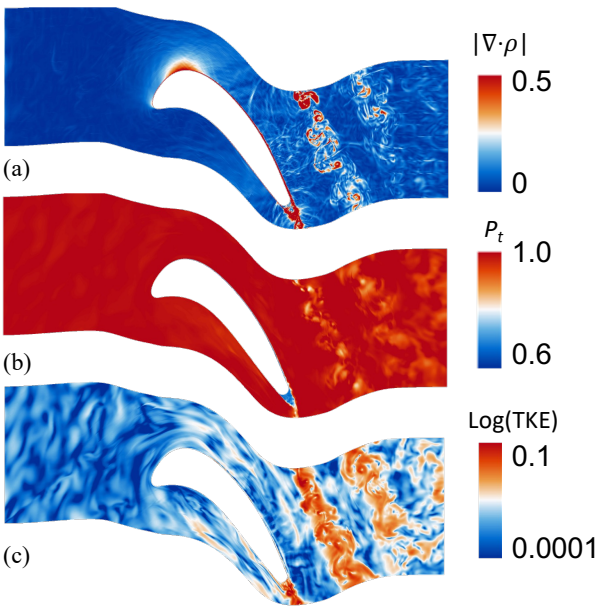


FIGURE 4: GRADIENT OF DENSITY, TOTAL PRESSURE, AND TOTAL TURBULENT KINETIC ENERGY AT THE MIDSPAN

calculations. The overall computational time for LES is about 150,000 CPUs.

Unsteady Flow Fields

Figures 4 (a)-(c) show the instantaneous profiles of the gradient of the normalized density, the total pressure and the total turbulent kinetic energy (TKE) (i.e., a sum of the resolved and unresolved turbulent kinetic energy) using the LES (50M) mesh. The small-scaled eddies generated at the inlet are propagating and elongated through an acceleration on the suction side. It is observed that the relatively large-scale turbulent structures remain in the downstream of the suction side. The boundary layer looks to be stable all along the suction side. Another interesting feature of using this blade with a large trailing edge diameter is to form a large recirculation zone. Unlike the low-Reynolds number case [9], this recirculation zone is not disturbed.

Figures 5 (a) and (b) show the instantaneous contours of the unresolved TKE using the LES (20M) mesh and LES (50M) mesh. When using the LES (20M) mesh, the stable laminar boundary layer is formed and then, the thick and wavy boundary layer edge develops. When using the LES (50M) mesh, the turbulent motions are resolved more. In fact, it is observed from Fig. 5 (b) that the unresolved TKE reduces. The suction side boundary layer appears to have transitioned into a turbulent boundary layer near the trailing edge, which is evidence by the sudden increase in the unresolved TKE (see the red-dotted circle in Fig. 5 (b)). In Figs. 6 (a) and (b), we compare the vorticity magnitude at different axial locations ($X/C_x = 0.75, 0.8, 0.85, 0.9, 0.95$ and 1.0) using two different grids. Although the profiles in the freestream region look similar to each other, there are some

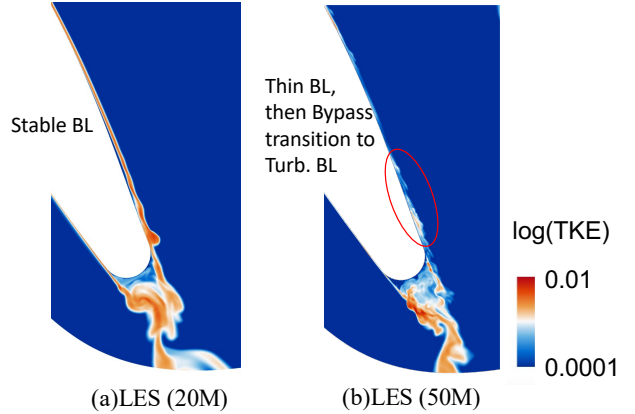


FIGURE 5: CONTOUR OF UNRESOLVED TURBULENT KINETIC ENERGY USING (a) LES (20M) and (b) LES (50M) MESHES

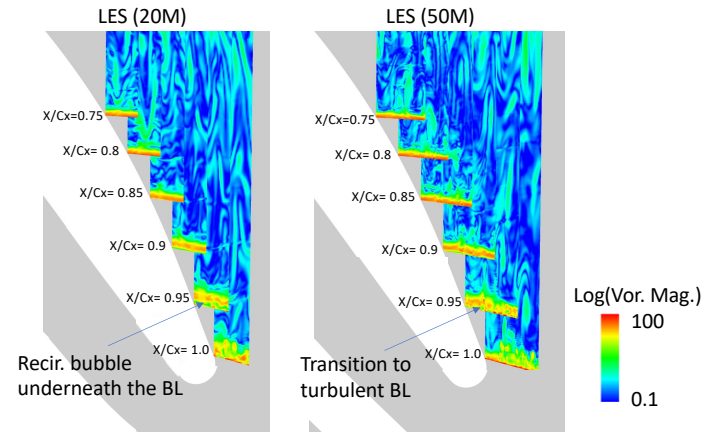


FIGURE 6: CONTOUR OF VORTICITY MAGNITUDE AT $X/C_x = 0.75, 0.8, 0.85, 0.9, 0.95$ and 1.0 USING (a) LES (20M) and (b) LES (50M) MESHES

noticeable differences in the vicinity of the wall. Increasing the grid count seems to resolve more active turbulent motions above the boundary layer (for instance, please compare two profiles at $X/C_x = 0.9$) As a result, the boundary layer seems to have been perturbed more. At $X/C_x = 0.95$, the transition to the turbulent boundary later takes place, and subsequently, a very thin, turbulent boundary layer is observed at $X/C_x = 1.0$. Using the LES (20M) mesh, there is a recirculation bubble underneath the boundary later at $X/C_x = 0.95$. In our previous studies [11], we demonstrated that when using a coarser mesh (or a lower-order scheme), boundary layer separation on the suction side occurs due to lack of turbulence production inside the boundary layer, which tends to be less resolved. In addition, the momentum transport from the free stream turbulence, which energizes the boundary layer, could be underestimated. Finally, although it is found that some of the large eddies are as large as the span, since the wake is spanwise uniform, it suggests that an increase of the computational domain in the span direction of the computational domain seems to have been unnecessary.

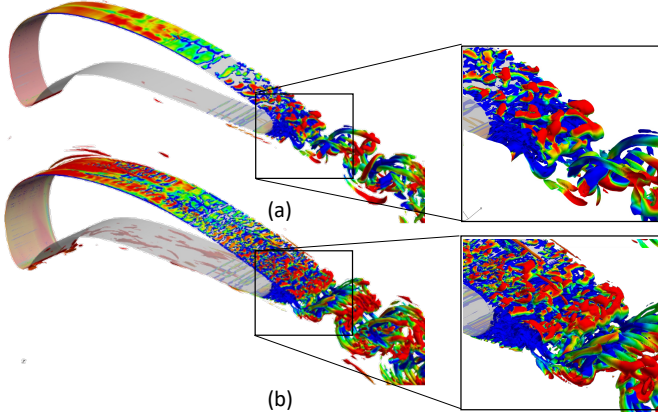


FIGURE 7: ISO-SURFACE Q-CRITERION COLORED BY NORMALIZED TOTAL PRESSURE (RED:1, BLUE:0.86) OF (a) LES (20M) and (b) LES (50M)

Figure 7 shows the three-dimensional view of the contour-surfaces of Q-criterion (=1) colored by the total pressure, which depict the transition phenomena near the trailing edge. There are distinct features such as vortex roll-up near the trailing edge and the hairpin vortices that are developed downstream. In the downstream region, the large structures (so-called Von Karman (V-K) vortices) are formed. When using the LES (50M) mesh (See Fig.7 (b)), there are much more small-scaled structures, which are coupled with the large structures. Also, it is observed that the small-scaled disturbances start developing further upstream and then break down near the trailing edge. This qualitatively confirms that bypass transition to the turbulent boundary layer takes place when the grid is further refined and not transition due to separation reattachment. There is no noticeable difference in the flow field in the spanwise direction. The flow in Fig. 7(b) shows that the large eddy structure in the wake is quite two-dimensional and that the eddy size is not changed from the 20M case. An increase in the grid resolution has had a noticeable impact on the small-scaled flow fields but not on the large-scaled flow fields. We conclude from the foregoing that the increase in the size of the span was not required and the refinement of the grid in the downstream/wake of the suction side is responsible for the improvements in the quality of the simulation.

Time-Averaged Flow Fields

In this subsection, we would like to check the time-averaged flow fields. Figure 8 shows the time-averaged dissipation functions (top) and the total pressure profiles (bottom) using the LES (20M) mesh and LES (50M) meshes. The dissipation function appears in the entropy transport equation and is related to the loss process. The dissipation function is evaluated for the compressible flow by:

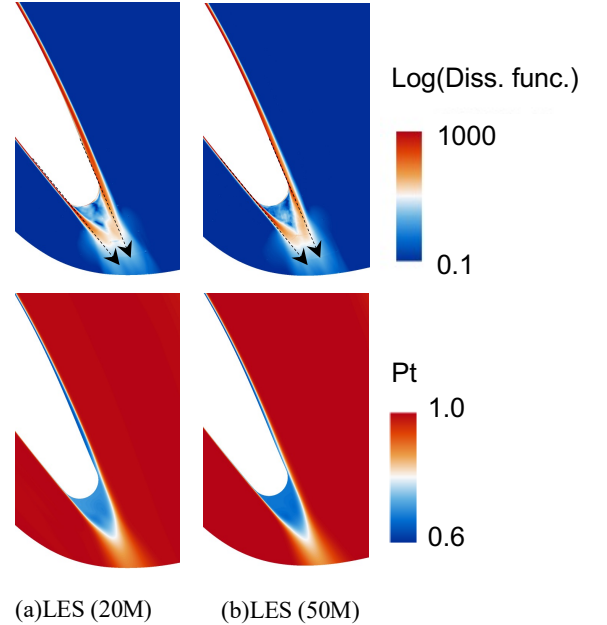


FIGURE 8: CONTOURS OF (TOP) DISSIPATION FUNCTION AND (BOTTOM) TOTAL PRESSURE OF (a) LES (20M) and (b) LES (50M)

$$\Phi = \frac{\mu}{2} \left(\frac{\partial u_i}{\partial x_j} + \frac{\partial u_j}{\partial x_i} \right)^2 - \frac{2\mu}{3} \left(\frac{\partial u_i}{\partial x_i} \right)^2 \quad (1)$$

Overall features of the dissipation functions predicted by two meshes are similar in the sense that the boundary layer losses from the pressure and suction sides merge in the downstream region. However, for the case with the LES (20M) mesh, the boundary layer loss from the suction side seems to be slightly larger (i.e., thicker red zone). This explains the larger blue region seen in the total pressure contour on the suction side when using the LES (20M) mesh. In addition, the thicker boundary layer predicted by using the LES (20M) mesh causes the point, where two boundary layers from the pressure and suction sides meet, to be shifted upward. This subtle shift can be seen by comparing two dashed arrows.

For a quantitative comparison between two flow fields, we calculated the normalized shear stress on the blade surface and axial velocity profiles at six selected locations ($X/C_x=0.9, 0.92, 0.94, 0.96, 0.98$, and 0.99) (see Fig. 9) using the LES (20M) and LES (50M) meshes. Both cases show very similar shear profiles both on the pressure side and suction sides except the end of the suction side. The case with the LES (20M) mesh shows zero shear stress between a: $X/C_x=0.9$ and c: $X/C_x=0.94$, which indicates that the flow is about to separate. And then, there is a small negative region where a recirculation bubble is located. The axial velocity profiles (blue line) shown on the top row of Fig. 9 clearly indicate the flow separation and the recirculation bubble between c: $X/C_x = 0.94$ and e: $X/C_x = 0.98$. It seems that the flow reattaches between e: $X/C_x = 0.98$ and f: $X/C_x = 0.99$. On

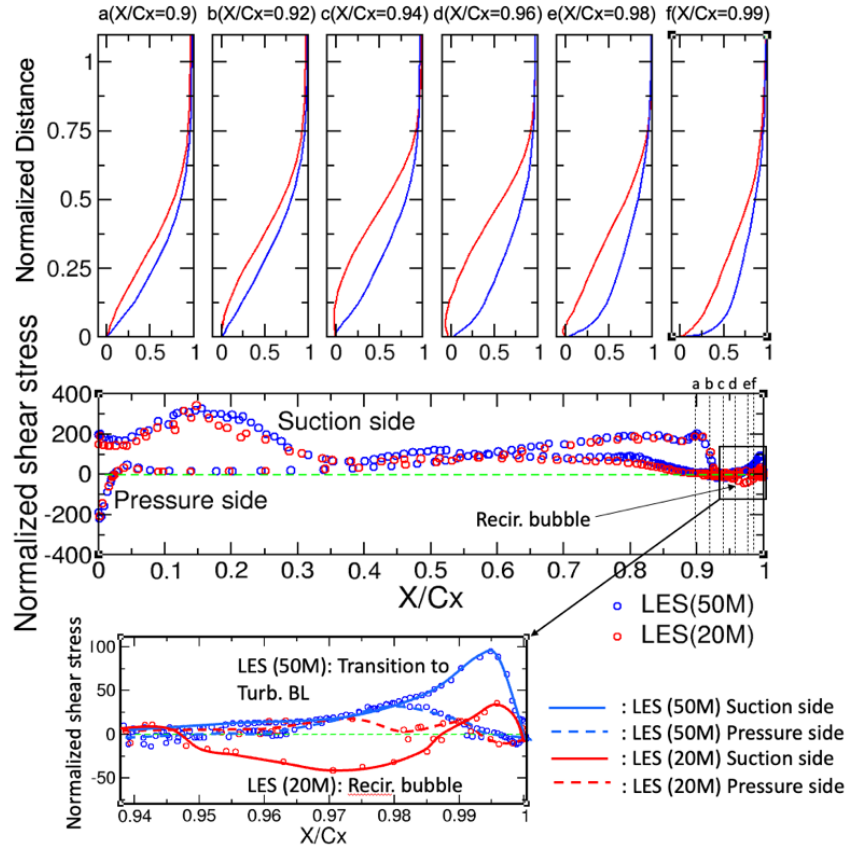


FIGURE 9: (TOP) TIME-AVERAGED NORMALIZED VELOCITY PROFULES (TOP) AT $X/C_x=0.9, 0.92, 0.94, 0.96, 0.98$ AND 0.99 AND (BOTTOM) SHEAR STRESS PROFILES OF RED: LES (20M) AND BLUE: LES (50M)

the other hand, when using the LES (50M) mesh, the shear stress remains positive and rapidly increases around d: $X/C_x = 0.96$, where the transition to the boundary layer takes place. As a result, the boundary layer appears fuller at f: $X/C_x = 0.99$. Looking at the velocity profiles from two meshes at f: $X/C_x = 0.99$, there are the flow angle to alter in the downstream region. In our past studies using the aft-loaded LPT blades [9], we also observed that using the denser grid can have a significant effect on the flow fields near the trailing edge by resolving momentum transfer from the freestream turbulence and production of TKE inside the boundary layer more. However, unlike the current study, the time-averaged shear stress and the pressure loading profiles did not indicate a small recirculation bubble. This study demonstrates that there is a more demanding mesh requirement (and the span) when modeling this type of a front-loaded blade in order to accurately capture the aerodynamic behaviors including the separation, reattachment, and transition near the trailing edge.

Finally, Figs. 10 (a) and (b) show the calculated pressure coefficients along the blade surface and the wake profiles at the midspan using the LES (20M) mesh (red) and the LES (50M) mesh (blue) with the experimental data. When using the newly generated mesh (blue line in Fig. 10 (a)), there is no kink associated with the separation bubble at $X/C_x = 0.95$. This

was one of the issues observed in our previous study [9]. Overall agreement with the experimental data is satisfactory. In Fig. 10 (b), there are three symbols from the data, depending on the blade location on the cascade. The predicted profile (blue line) gets close to the data (i.e., less shifted), and thus the peak location matches the data within the experimental uncertainty. As shown in Fig. 8 (and Fig. 9), the flow field at the end of the suction side is more energized through the momentum transfer from the free-stream turbulence and the turbulent production inside the boundary layer using the denser grid. This slightly changes the direction of the shear layer departing from the trailing edge. To qualitatively compare these wake profiles, we evaluated the area-averaged kinetic energy loss coefficients, e_2 and found that the predicted e_2 by both meshes are 0.0438 for LES (20M) and 0.0414 for LES (50M), which are very close to the data ($=0.042$).

CONCLUSIONS

We utilized LES to calculate the pressure loading profile, the total loss distribution, and the integrated pressure loading profile of the front-loaded CMC blade at the high-freestream turbulence ($Tu=13\%$). In order to resolve the issues reported in our previous studies [9] (a small recirculation bubble at the end of the suction side and the ‘‘shifted’’ wake profile),

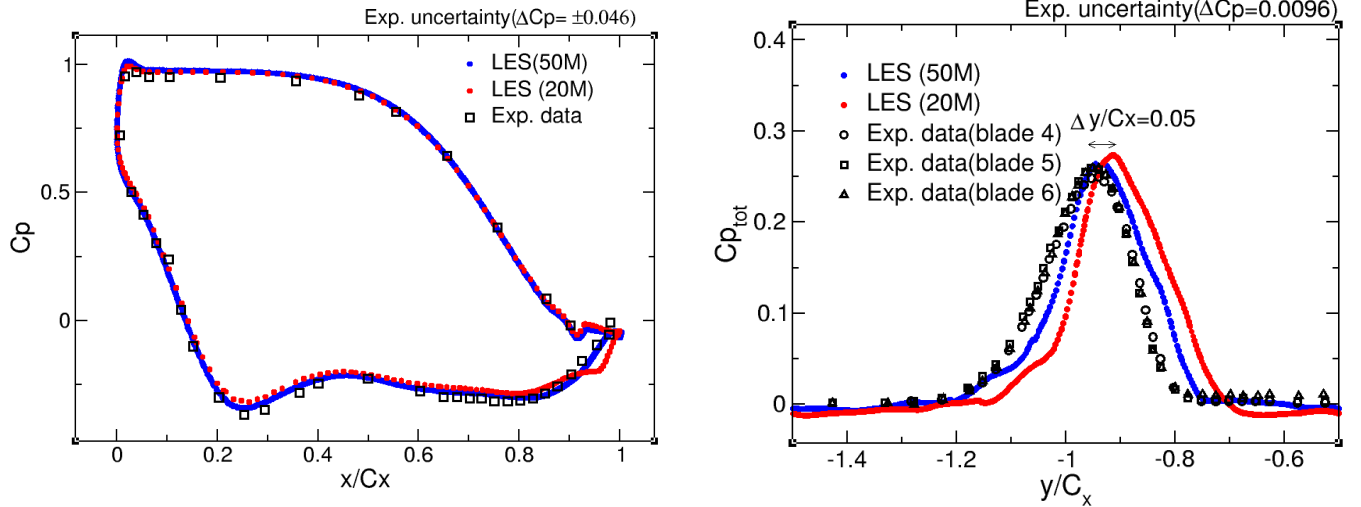


FIGURE 10: (a) PRESSURE LOADING ON THE BLADE AT THE MIDSPAN AND (b) TOTAL PRESSURE LOSS COEFFICIENT IN THE WAKE ($X/C_x=1.2$) USING THE LES (20M) [9] GRID (RED) AND THE LES (50M) MESH (BLUE).

we newly generated the mesh by increasing the resolution near the trailing edge and expanding the span. Using the finer mesh covering a larger span, there is no recirculation bubble observed. It is because the flow is energized by the momentum transfer from the freestream turbulence and more resolved turbulent production. As a result, the transition to the turbulent boundary layer (Bypass transition) takes place. This effect on the transition mechanism is attributed to the local resolution of the grid in the trailing edge region and not attributed to the increase in the span of the blade which we found to have had no noticeable effect on the solution. In addition, the fuller velocity profile alters the direction of the shear layer departing from the trailing edge, which improves the shift of the wake profile.

This study revisited the importance of the mesh requirements for LES. The requirement could be stricter than the suggested one for LES simulations [11] when modeling a blade design, which prompts the flow to separate on the suction side. Local refinement of the mesh near the end of the suction side appears to be a good practical resolution.

ACKNOWLEDGEMENTS

This work was supported by Ms. Reinert Jessica for the NASA Advanced Air Transport Technology project. Experimental data was provided by Dr. Paul Giel, which is appreciated. The authors also would like to thank Dr. David Rigby and Dr. Erlendur Steinhorsson for their assistance in preparing and running the simulations. The simulations were conducted on the NASA Advanced Supercomputing (NAS) Pleiades computer cluster.

REFERENCES

[1] Giel, P., Shyam, V., Juangphanich, P., and Clark, J.P., 2020, "Effects of Trailing Edge Thickness and Blade Loading

Distribution on the Aerodynamic Performance of Simulated CMC Turbine Blades," Proceedings of the ASME Turbo Expo, Virtual, GT2020-15802.

[2] Lyall, M. E., King, P., Sondergaard, R. S., and Clark, J., 2012, "An Investigation of Reynolds Lapse Rate for Highly Loaded Low Pressure Turbine Airfoils With Forward and Aft Loading," Journal of Turbomachinery: 134, p. 051035-1.

[3] Keadle, K., and McQuilling, M., 2013, "Evaluation of RANS Transition Modeling for High Lift LPT Flows at Low Reynolds Number," Proceedings of the ASME Turbo Expo, Virtual, San Antonio, TX, USA, June 20013, GT2013-95069.

[4] Arko-, B., and McQuilling, M., 2013, "Computational Study of High-Lift Low-Pressure Turbine Cascade Aerodynamics at Low Reynolds Number," Journal of Propulsion and Power: 29, 446-459

[5], Vazquez, R., Antoranz, A., Cadrecha, D., and Armananzas, L., 2016, "The Influence of Reynolds Number, Mach Number and Incidence Effects on Loss Production in Low Pressure Turbine Airfoils," ASME Turbo Expo, Barcelona, Spain, May 2006, GT2006-91121

[6] Medic, G., Sharma, O., 2012, "Large-Eddy Simulation of Flow in a Low-Pressure Turbine Cascade," Proceedings of the ASME Turbo Expo, Copenhagen, Denmark, June 2012, GT2012-68878

[7] Bolinches-Gisbert, M., Robles, D.C., Corral, R., and Gisbert., 2020, "Prediction of Reynolds Number Effects on Low-Pressure Turbines Using a High-Order ILES Method," Journal of Turbomachinery: 142, p 031002.

[8] Pichler, R., Sandberg, R.D., Michelassi, V., "Assessment of Grid Resolution Requirements for Accurate Simulation of Disparate Scales of Turbulent Flow in Low-Pressure Turbines," Proceedings of the ASME Turbo Expo, GT2016-56858

[9] Miki, K., Ameri, A., 2022, "Numerical Investigation of the Effect of Trailing Edge Thickness of Simulated CMC Blades

on Loss Profiles ,” Proceedings of the ASME Turbo Expo, Rotterdam, Netherlands, June 2022, GT2022-82335

[10] Ameri, A., 2016, “Requirements for LES Computations of VSPT Flows”, NASA CR-2016-218962.

[11] Miki, K., Ameri, A., 2021, “Improved Prediction of Losses with Large Eddy Simulation in a Low-Pressure Turbine,” Journal of Turbomachinery, (in print), TURBO-21-1207 doi.org/10.1115/1.4053234.

[12] Thurman, D., Flegel, A., Giel, Pau., 2014, “Inlet Turbulence and Length Scale measurements in a Large-Scale Transonic Turbine Cascade,” Proceedings of the 50th AIAA Joint Propulsion Conference, AIAA 2014-3934.

[13] Steinthorsson, E., Liou, M-S. Povinelli, L., 1993, “Development of an Explicit Multiblock/Multigrid Flow Solver for Viscous Flows in Complex Geometries,” Proceedings of the 29th Joint Propulsion Conference and Exhibit, AIAA Paper 1993-2380.

[14] Liou, M.-S., 2006, “A Sequel to AUSM, Part II: AUSM+-up for All Speeds,” Journal of Computational Physics: 214, p 137-170.

[15] Kim, W.-W. Menon, S., 1995, “A New Dynamic One-equation Subgrid-scale Model for Large Eddy Simulations,” Proceedings of the 33rd AIAA Aerospace Sciences Meeting and Exhibit, January 1995, AIAA Paper 1995-356.

[16] Lilly, D. K., 1992, “A Proposed Modification of the Germano Subgrid-scale Closure Method”, Physics of Fluids: 4, 633-635.

[17] Miki, K., Ameri, A., 2020, “Large-Eddy Simulation of The Variable Speed Power Turbine Cascade with Inflow Turbulence,” Journal of Turbomachinery: 143, No 8.

[18] Miki, K., Ameri, A., 2021, “Improved Prediction of Losses with Large Eddy Simulation in a Low-Pressure Turbine,” Journal of Turbomachinery, (in print), TURBO-21-1207 doi.org/10.1115/1.4053234.

[19] Klein, M., Sadiki, A., Janicka, J., 2003, “A Digital Filter Based Generation of Inflow Data for Spatially Developing Direct Numerical or Large Eddy Simulations”, Journal of Computational Physics: 186, 652-665.

[20] Lee, Y., Teramoto, S., Toki, T., Okamoto, K., 2020, “Effect of the large Eddy Simulation Calculation Parameters on Prediction of Profile Loss in an Axial Cascade at Off-Design Incidence”, Proceedings of the ASME Turbo Expo, Virtual, September, GT2020-14554.